Relative depolarization of the black hole photon ring in GRMHD models of Sgr A* and M87*

Jiménez-Rosales, A.; Dexter, J.; Ressler, S.M.; Tchekhovskoy, A.; Bauböck, M.; Dallilar, Y.; ... ; Widmann, F.

Relative depolarization of the black hole photon ring in GRMHD models of Sgr A* and M87*

A. Jiménez-Rosales,[1,2]⋆ J. Dexter,[3,2]† S. M. Ressler,[4] A. Tchekhovskoy,[5] M. Bauböck,[2] Y. Dallilar,[2] P. T. de Zeeuw,[2,6] A. Drescher,[2,7] F. Eisenhauer,[2] S. von Fellenberg,[2] F. Gao,[2] R. Genzel,[2,8] S. Gillessen,[2] M. Habibi,[2] T. Ott,[2] J. Stadler,[2] O. Straub,[2] F. Widmann[2]

[1]*Department of Astrophysics, IMAPP, Radboud University, 6500 GL Nijmegen, The Netherlands*
[2]*Max Planck Institute for Extraterrestrial Physics (MPE), Giessenbachstr. 1, 85748 Garching, Germany*
[3]*JILA and Department of Astrophysical and Planetary Sciences, University of Colorado, Boulder, CO 80309, USA*
[4]*Kavli Institute for Theoretical Physics, University of California Santa Barbara, Kohn Hall, Santa Barbara, CA 93107, USA*
[5]*Center for Interdisciplinary Exploration & Research in Astrophysics (CIERA), Physics & Astronomy, Northwestern University,*
Evanston, IL 60202, USA
[6]*Sterrewacht Leiden, Leiden University, Postbus 9513, 2300 RA Leiden, The Netherlands*
[7]*Department of Physics, Technical University Munich, James-Franck-Straße 1, 85748 Garching, Germany*
[8]*Departments of Physics and Astronomy, Le Conte Hall, University of California, Berkeley, CA 94720, USA*

ABSTRACT
Using general relativistic magnetohydrodynamic simulations of accreting black holes, we show that a suitable subtraction of the linear polarization per pixel from total intensity images can enhance the photon ring features. We find that the photon ring is typically a factor of $\simeq 2$ less polarized than the rest of the image. This is due to a combination of plasma and general relativistic effects, as well as magnetic turbulence. When there are no other persistently depolarized image features, adding the subtracted residuals over time results in a sharp image of the photon ring. We show that the method works well for sample, viable GRMHD models of Sgr A* and M87*, where measurements of the photon ring properties would provide new measurements of black hole mass and spin, and potentially allow for tests of the "no-hair" theorem of general relativity.

Key words: accretion, accretion discs — black hole physics — MHD — polarization — radiative transfer

1 INTRODUCTION

Long baseline interferometry techniques have the power to resolve and explore the innermost regions of accretion flows around supermassive black holes. Interferometric measurements made with GRAVITY at the Very Large Telescope (Eisenhauer et al. 2008; Paumard et al. 2008; Gravity Collaboration et al. 2017) and the Event Horizon Telescope (EHT; Doeleman et al. 2008, 2012; Fish et al. 2011), have offered unprecedented capability to study these systems at angular scales of tens of microarcseconds (μas). That resolution is comparable to the size of the event horizon on the sky for the Galactic center black hole, Sagittarius A* (Sgr A*), and the supermassive black hole in M87, M87*. The observations probe not only the geometrical and physical properties of matter around the compact object, but also allow for tests in the strong-field regime of general relativity (Gravity Collaboration et al. 2018a,b, 2020a,b; Event Horizon Telescope Collaboration et al. 2019a,b,c,d,e,f).

Theoretical studies of low-luminosity accretion onto black holes encompass analytic models (e.g., Ichimaru 1977; Rees 1982; Narayan & Yi 1994; Yuan et al. 2003), semi analytic calculations (e.g., Falcke et al. 2000; Bromley et al. 2001; Broderick & Loeb 2005, 2006) and numerical simulations. The latter include general relativistic magnetohydrodynamic (GRMHD) calculations, where the equations of ideal magnetohydrodynamics are written, solved and self-consistently evolved taking into account general relativistic effects (e.g., Gammie et al. 2003; De Villiers et al. 2003; Noble et al. 2006; Tchekhovskoy et al. 2011; Narayan et al. 2012; Shiokawa 2013).

While predicted total intensity images of emission arising at event horizon scales are useful in studying the properties of the accretion flow (e.g. size, shape, variability; Dexter et al. 2009; Mościbrodzka et al. 2009; Chan et al. 2015; Anantua et al. 2020; Dexter et al. 2020), they are often dominated by light bending and Doppler boosting. Polarization information has proven to be

⋆ a.jimenez@science.ru.nl
† jason.dexter@colorado.edu

a key element in complementing these studies, setting limits on model quantities such as accretion rate and electron temperature from observables like linear polarization fraction (e.g., Aitken et al. 2000; Agol 2000; Quataert & Gruzinov 2000; Bower et al. 2017), rotation measure (Bower et al. 2003; Marrone 2006; Marrone et al. 2007; Kuo et al. 2014; Bower et al. 2018) and spatially resolved magnetic field structure (e.g., Johnson et al. 2015; Mościbrodzka et al. 2017; Jiménez-Rosales & Dexter 2018; Gravity Collaboration et al. 2020c).

The emission around a black hole is gravitationally lensed. At event horizon scales, the strength of this effect is such that it produces a sequence of strongly lensed images of the surrounding emission (e.g., Cunningham & Bardeen 1973; Luminet 1979; Viergutz 1993) that result in an annulus of enhanced brightness (we henceforth refer to all indirect images as the "photon ring"). Analytic studies show that if the emission around the black hole is optically thin, the photon ring may show universal features both in total intensity and polarization that are completely governed by general relativity (Johnson et al. 2019; Himwich et al. 2020).

The EHT Collaboration's published images of M87* show a bright ring of emission surrounding a dark interior (Event Horizon Telescope Collaboration et al. 2019d). The presence of a photon ring is expected within this emission, surrounding the black hole shadow (Falcke et al. 2000). Measuring its properties, including the size and shape, provide new measurements of the mass and spin of the black hole and could even test the "no-hair" theorem of general relativity (e.g., Johannsen & Psaltis 2010). Typically, the photon ring contributes $\simeq 5 - 10\%$ of the total flux in GRMHD models (e.g., Ricarte & Dexter 2015). The challenge is to separate this feature from surrounding direct emission. Psaltis et al. (2015) showed that the edge of the photon ring feature is generally sharp, which may help with its extraction. This may also be possible using extremely long baselines (e.g., with one telescope in space), if stochastic source features can be smoothed by coherently averaging (Johnson et al. 2019).

Here, we use GRMHD calculations to show that the polarized radiation may provide another method. In many current GRMHD models, the photon ring is enhanced when suitably subtracting the linear polarized flux per pixel from the total intensity (Section 2). We find that the photon ring is persistently less polarized relative to rest of the image by a factor of $\simeq 2 - 2.5$ (Section 3). The relative depolarization is due to a combination of plasma and general relativistic effects, as well as magnetic field disorder. We discuss our results and conclude in Section 4.

2   PHOTON RING EXTRACTION

In this work we use two long duration, 3D GRMHD simulations of black hole accretion flows described in Dexter et al. (2020): one in a strongly magnetized (magnetically arrested disc, MAD) regime and the other in a weakly magnetized (standard and normal evolution, SANE) one. The simulation's framework allows for the independent, self-consistent evolution of four electron internal energy densities in pair with that of the single MHD fluid (Ressler et al. 2015). Here, we use a turbulent heating prescription based on gyrokinetic theory (H10, Howes 2010) for the MAD model and electron heating in magnetic reconnection events from particle-in-cell simulations (W18, Werner et al. 2018) for the SANE model.

Both simulations are run with the HARMPI[1] code (Tchekhovskoy 2019). The initial condition is that of a Fishbone-Moncrief torus (Fishbone & Moncrief 1976) with inner radius at $r_{in} = 12\,r_g$ ($r_g = GM/c^2$), pressure maximum radius $r_{max} = 25\,r_g$, threaded with a single poloidal loop of magnetic field and black hole spin parameter of $a = 0$ and $a = 0.9375$ for the SANE and MAD cases respectively.

In the MAD case, the simulation was run for a time of $6 \times 10^4\,r_g/c$, each snapshot spaced by $10\,r_g/c$, establishing inflow equilibrium out to $r \simeq 90\,r_g$. In the SANE case, the simulation is studied at late times ($1.7 \times 10^4\,r_g/c$, each snapshot spaced by $10\,r_g/c$ as well), once radii $r \gtrsim 100\,r_g$ have reached inflow equilibrium. By doing this, we avoid "artificial" depolarization in the images from external Faraday rotation from zones far out in the accretion flow that are not yet in equilibrium. See Dexter et al. (2020) for more details.

We calculate post-processed images using the general relativistic ray-tracing public code GRTRANS[2] (Dexter & Agol 2009; Dexter 2016). The electron temperature is taken directly from the GRMHD electron internal energy density, $kT_e = (\gamma_e - 1)m_p u_e/\rho$, where we use $\gamma_e = 4/3$ and have assumed a composition of pure ionized hydrogen. The mass of the black hole is set to $4 \times 10^6\,\mathrm{M}_\odot$, where $\mathrm{M}_\odot$ indicates the solar mass unit, and the mass accretion rate is scaled until the observed flux density at 230 GHz matches that of Sgr A* at this frequency ($\simeq 3$ Jy, e.g., Dexter et al. 2014; Bower et al. 2015). In our calculations, we exclude emission from regions where $\sigma = u_B/\rho c^2 > 1$, with $u_B = b^2/4\pi$ the magnetic energy density. We calculate observables at 230 GHz and a viewing orientation of $i = 50$ degrees. The image resolution is 192 pixels over a $42\,r_g$ ($\sim 210\,\mu$as) field of view (a discussion of resolution effects can be found in Appendix A).

Panels 1 and 2 in the top and bottom rows of Fig. 1 show total intensity (Stokes I) and linear polarized flux, $LP = \sqrt{Q^2 + U^2}$, of snapshot images of the MAD and SANE simulations respectively, where the Stokes parameters Q and U denote the linear polarization states at 0/90 and ±45 degrees at each pixel. In both cases, the total intensity and linear polarized flux images exhibit similar morphologies. We note as well that the images present a sharp, bright photon ring with many depolarized areas on it. The net linear and circular polarization fractions (LPf[3] and CPf[4] respectively) in the image are indicated in Panel 2.

Suitably subtracting the polarized flux from the total intensity per pixel results in a residual image with a clearer photon ring. We introduce a scaling factor f that accounts for the difference between the image's polarized flux and total intensity[5]. The residual image is then $I - 1/f\,LP$. An example of the "instantaneous" (one snapshot) residuals for the values shown in Panels 1 and 2 is shown in Panel 3 in the top and bottom rows of Fig. 1. Here we have run through a set of values of f (0.3 − 1.0 spaced every 0.05 and $f = \langle LP \rangle/\langle I \rangle$) and chosen the value which minimizes the sum of the residuals outside of a thin ring on the sky with a width from $4.8 - 5.5\,r_g$. This is close to expected position of the photon ring ($\sqrt{27}\,r_g$ for a Schwarzschild black hole and $\simeq 5\,r_g \pm 4\%$ and nearly circular

---

[1] https://github.com/atchekho/harmpi

[2] https://github.com/jadexter/grtrans

[3] LPf=$\sqrt{\langle Q \rangle^2 + \langle U \rangle^2}/\langle I \rangle$, where $\langle \rangle$ denotes the sum over all pixels.

[4] CPf=$\langle V \rangle/\langle I \rangle$, with V the circular polarization Stokes parameter.

[5] Since light might not be completely linearly polarized, $I \geq LP$, so that $\langle I \rangle \geq \langle LP \rangle$. To account for this difference, the factor f should then be similar to $\langle LP \rangle/\langle I \rangle$.
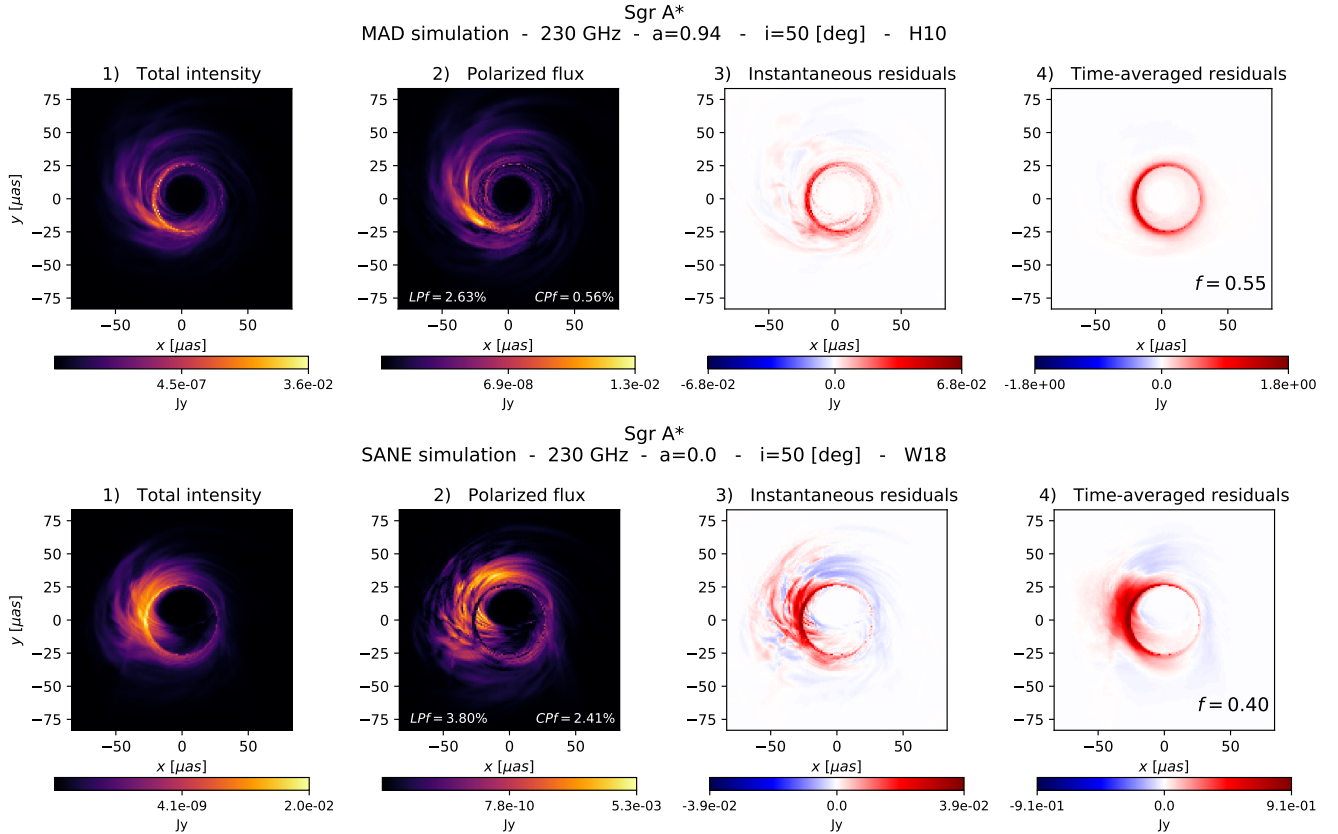
Figure 1. Total intensity, polarized flux and residual images of Sgr A* at 230 GHz. Top row: MAD simulation with spin $a = 0.94$, inclination $i = 50°$ and turbulent electron heating (H10). Bottom row: SANE simulation with spin $a = 0.0$, inclination $i = 50°$ and magnetic reconnection as the electron heating mechanism (W18). Panels 1 and 2 show respectively the total intensity I and the polarized flux LP for a snapshot of the simulations. Emission is shown in false color. Higher emission zones are denoted by lighter colors. Both images exhibit similar morphologies, with the difference that the polarized flux image has many more dark areas in the accretion flow due to depolarization. The photon ring is a prominent feature in both and appears less polarized compared to the rest of the image. The net fractional LP and CP in the image are indicated in Panel 2. 3) Instantaneous residuals $I - 1/f\ LP$ for a snapshot. 4) Time-averaged residuals over thirty frames. The snapshots are separated by 10 GM/c^3. If the depolarized image features change over time except at the photon ring, the residuals average out everywhere else, enhancing the ring in the residual image. The factor f indicated at the bottom of panel 4 is such that the residuals in the image are minimized.

across all spins, Johannsen & Psaltis 2010) and where most of the emission is contained. In our calculations we consider as "photon ring pixels" those that lie within this ring. The images are inspected to ensure that all of the photon ring pixels are included. Save for small translations of the center of the ring due to spin changes between the simulations, the pixel selection radii remains the same. Note that our definition of photon ring pixels includes foreground "contamination" from the direct image, but this is generally a minor contribution.

The total intensity and LP images vary in time due to turbulent fluctuations in the accretion flow. These variations are strongly correlated, except that the LP image varies somewhat more. This is because the direction of the polarization vector depends strongly on the underlying magnetic turbulence and/or Faraday effects, resulting in transient depolarization of some image pixels. The photon ring, however, remains visible and less polarized over time. The stability of the photon ring properties implies that the extraction technique benefits from source variability. Adding residual images tends to average out the residuals everywhere but the photon ring, increasing its contrast. Panel 4 in the top and bottom rows of Fig. 1 shows the cumulative residual images over thirty frames of our simulations

for each case, starting from $5.1 \times 10^3\ r_g/c$ for the MAD simulation and $1.7 \times 10^4\ r_g/c$ for the SANE simulation. This corresponds to a time span of ~ 1.7 hr for Sgr A* and ~ 100 days for M87*. The best f value that minimizes the residuals in the time-averaged image is indicated in panel 4. It can be seen that an optimal choice of f leads to the residuals successfully averaging out over time, sharpening the photon ring.

3 NUMERICAL PROPERTIES OF THE PHOTON RING

We investigate the reasons for which the photon ring has different properties from the rest of the image. To do this, we study how the polarization properties of the photon ring are affected in the presence/absence of effects that can depolarize an image. We consider four effects: absorption, Faraday rotation and conversion, magnetic turbulence and parallel transport.
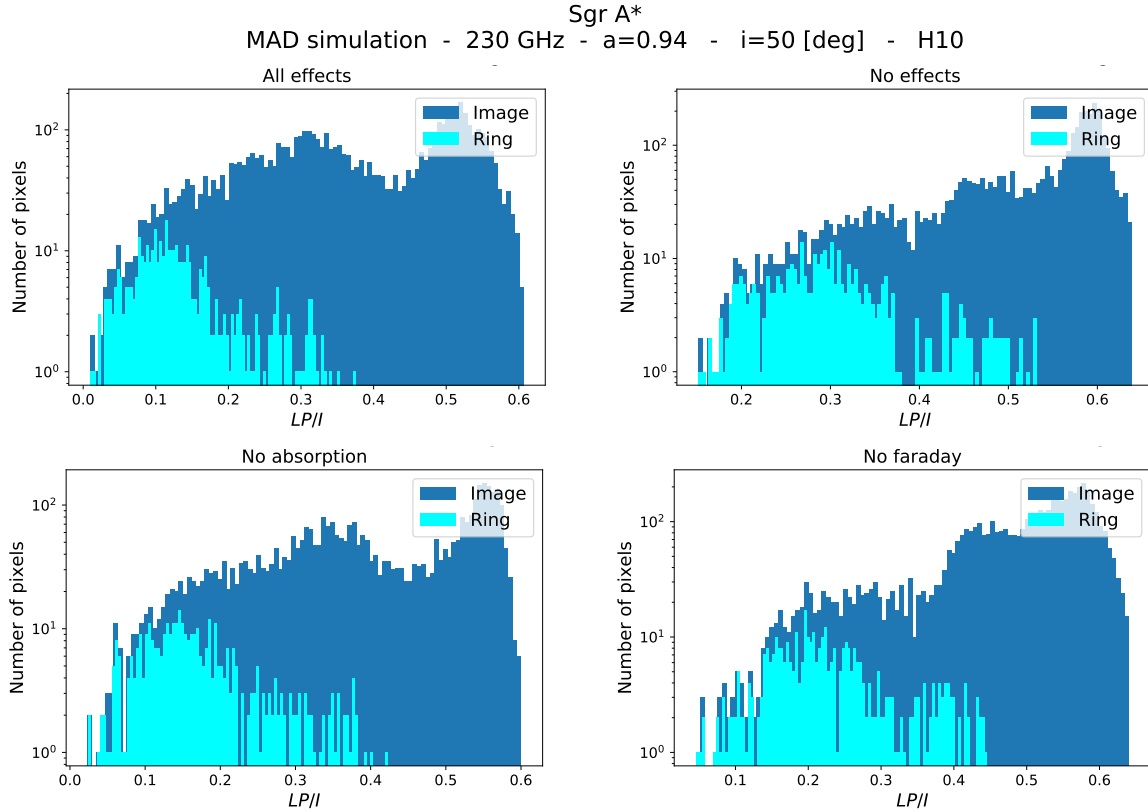
Figure 2. Distribution of image and ring fractional polarized flux (LP/I) per pixel for the MAD simulation. Only pixels with a total intensity of at least 10% I_{med} are considered, with I_{med} the median of the one hundred brightest pixels. Image pixels are in dark blue, ring pixels are in cyan. LP/I is calculated from thirty-frame averaged images where different effects are considered. Top left: all effects. Top right: no effects. Bottom left: no absorption. Bottom right: no Faraday effects. In all cases the photon ring pixels are preferentially less polarized relative to the rest of the image.

3.1 Effects of absorption, Faraday rotation and Faraday conversion

GRTRANS calculates images by solving the polarized radiative transfer equation along geodesics traced between where a photon was emitted and the observer's camera. By setting the absorption, Faraday rotation or conversion coefficients in the radiative transfer equation to zero, we can study the influence of these effects straightforwardly.

We first look at the distribution of LP/I in the image and photon ring pixels from a set of images where either all (or none) of the effects have been taken into account. In order to avoid biases from dim regions in the image, only pixels with a total intensity of at least 10% I_{med} have been considered, with I_{med} the median of the one hundred brightest pixels.

Figures 2 and 3 show that the photon ring is a clear outlier in the distribution of polarized flux in all cases. When absorption and/or Faraday rotation are neglected, the polarization fraction increases everywhere. Still the photon ring remains fairly less polarized compared to the rest of the image.

The net fractional LP in the ring and image is given by $m_x = \langle LP/I \rangle$ where x denotes whether the calculation uses image or photon ring pixels. The values of m for the MAD and SANE cases are shown in Tables 1 and 2. In all cases the photon ring is about a factor of $\simeq 2 - 2.5$ less polarized than the rest of the image, with maximum depolarization obtained when all effects are included in the calculations. As expected, the highest degree of polarization in

Table 1. Image and ring net fractional LP (m) of the MAD simulation. The values are calculated from a thirty-frame averaged image including effects of absorption and/or Faraday rotation and conversion at a time.

		All effects	No effects	No absorption	No Faraday
MAD	m_{Image} [%]	44.66	51.89	47.88	48.23
	m_{Ring} [%]	20.73	32.45	27.46	23.94
	m_{Ring} / m_{Image}	0.46	0.63	0.57	0.50

Table 2. Image and ring net fractional LP (m) of a thirty-frame averaged SANE image with different effects included in the calculations.

		All effects	No effects	No absorption	No Faraday
SANE	m_{Image} [%]	30.87	53.69	48.56	43.79
	m_{Ring} [%]	18.00	39.76	35.77	25.94
	m_{Ring} / m_{Image}	0.58	0.74	0.74	0.59

the ring ($\sim 60 - 75\%$ of that of the image) is achieved when neither effect is included in the calculation. Absorption has a larger impact on the depolarization degree of the ring than Faraday effects (about $\sim 10\%$ more). However, neither effect alone (or combined) amounts to the total observed level of depolarization in the photon ring. A comparison between the "all effects" and "no effects" cases shows that for these simulations the plasma effects decrease the relative fractional polarization in the ring, m_{Ring}/m_{Image}, by $\sim 20\%$, while other effects do so by $\sim 30\%$.
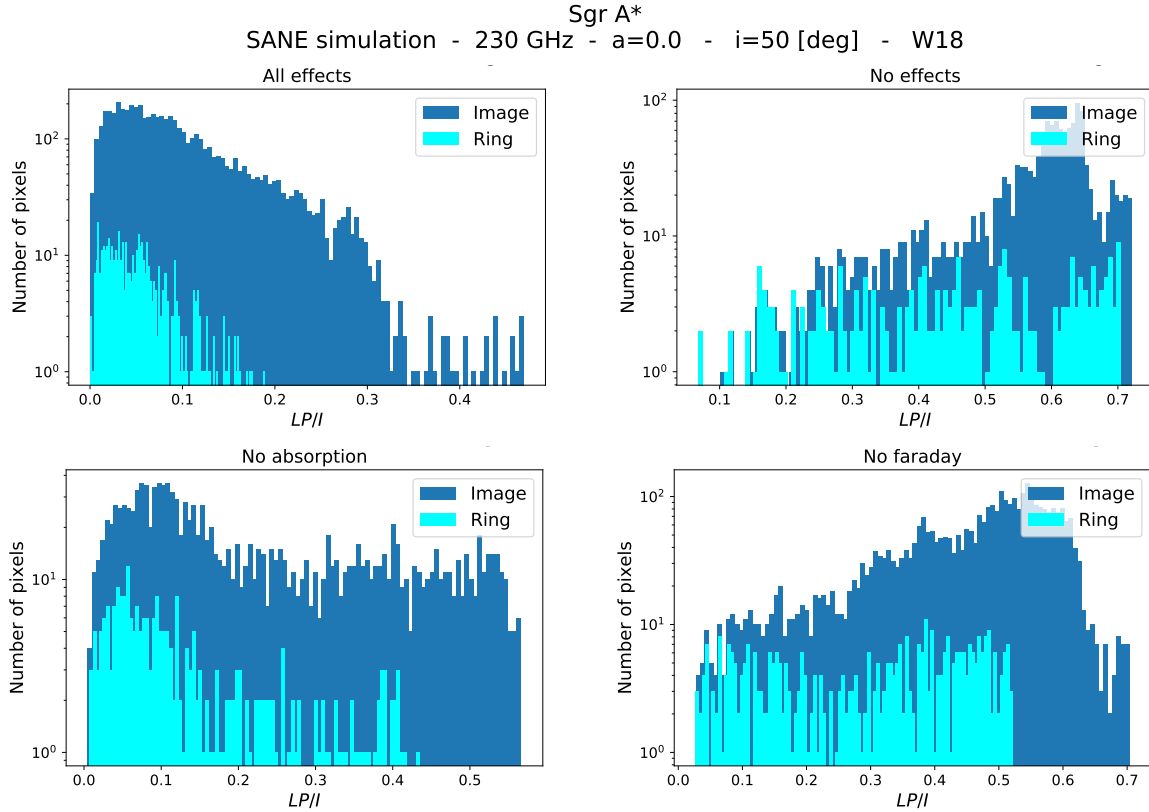
Figure 3. Distribution of LP/I per pixel for the SANE simulation. Only pixels with a total intensity of at least 10% I_{med} are considered, with I_{med} the median of the one hundred brightest pixels. The values are calculated from thirty-frame averaged images where different effects are considered. Image pixels are in dark blue, ring pixels are in cyan. Top left: all effects. Top right: no effects. Bottom left: no absorption. Bottom right: no Faraday effects. Just like in the MAD case, the photon ring pixels are clear outliers in the distribution.

3.2 Effects of magnetic turbulence and parallel transport

We next look into the effects of magnetic field turbulence and gravitational effects. We expect magnetic field turbulence and parallel transport to depolarize emission in the ring due to multiple contributions to the polarized intensities $j_{Q,U}$ along the light rays (which wrap around the black hole), which will tend to average down. However, while parallel transport is constant in time and model independent, magnetic field structure can be vastly different in models and exhibit time dependent behaviour.

In order to study turbulent magnetic field structure effects more, we compare our MAD and SANE GRMHD results to idealized semi-analytical models with an ordered magnetic configuration and no radiative transfer effects. We consider an optically-thin compact emission region ("hotspot", Broderick & Loeb 2006) orbiting a black hole. The hotspot is moving with constant speed (matching that of a test particle at its center) in the equatorial plane at orbital radius R_0. We consider two magnetic field geometries, vertical and toroidal; two different orbital radii, $4\ r_g$ and $8\ r_g$; and three black hole spins, $a = -0.9, 0.0, 0.9$. The maximum particle density $n_{spot} \sim 2 \times 10^7\ cm^{-3}$ falls off as a 3D Gaussian with characteristic size R_{spot}. We fix the viewer's inclination at $i = 50$ degrees, consistent with GRAVITY flare observations (Gravity Collaboration et al. 2018b, 2020a,c). We calculate synchrotron radiation from a power law distribution of electrons with a minimum Lorentz factor of 1.5×10^3.

Example images of total intensity and polarized flux of one of

the models are presented in panels 1 and 2 of Fig. 4. The panels show stacked images over one revolution of the hotspot. The orbital radius is $R_0 = 4\ r_g$, the black hole spin $a = 0.0$ and the magnetic field geometry is completely vertical. Since the emission is subject to no effects other than magnetic field structure and gravitational effects, there is a lack of dark depolarized zones in the LP image. We can see gravitational lensing and beaming in the form of secondary images, asymmetry in the emission (top brighter than bottom due to Doppler beaming from the hotspot approaching the observer) and the photon ring.

The distribution of fractional LP per pixel in the idealized model (right panel of Fig. 4) shows that the photon ring pixels have a similar behaviour to that of the rest of the image. This is supported by the m values (Table 3). Similar results are found for the rest of the models.

In contrast to the MAD and SANE cases, $m_{Ring} \simeq m_{Image}$ in the hotspot models, which suggests that complex magnetic field structure is an important factor for depolarizing the photon ring.

Tables 1 and 2 show that generally speaking, the SANE simulation is more depolarized than the MAD (up to $\sim 60\%$ depolarization with respect to the rest of the image when all effects are considered). Comparing both "no effects" cases for the MAD and SANE simulation, where no radiative transfer effects are included in the calculations, we see that their net polarized fluxes have very similar values. In the SANE case the weak fields are sheared into a predominantly toroidal configuration in the accretion flow, while in the MAD case significant poloidal components remain. While
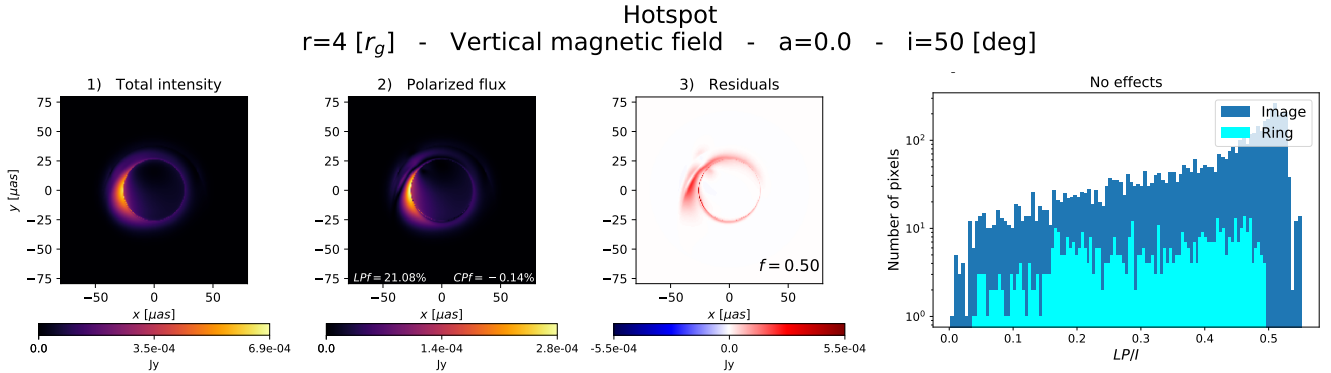
Figure 4. Stacked frames of a hotspot orbiting the black hole with spin $a = 0.0$. The hotspot is at a distance $4\ r_g$, traces clockwise motion and moves in a completely vertical magnetic field. The observer's inclination angle is $i = 50°$. In this simplified model the magnetic field is fully ordered and both self-absorption and Faraday rotation are negligible. 1) Total intensity. 2) Polarized flux. 3) Residual image. 4) Distribution of LP/I of the image and photon ring pixels. Only pixels with a total intensity of at least 10% I_{med} are considered, with I_{med} the median of the one hundred brightest pixels. Image pixels are in dark blue, ring pixels are in cyan. Unlike the MAD and SANE cases, the photon ring pixels follow a similar distribution compared to the rest of the image.

Table 3. Net fractional LP (m) of stacked images over one revolution of a hotspot model in different magnetic field (B) geometries.

Hotspot	B field	Spin	m_{Image} [%]	m_{Ring} [%]	$m_{Ring}\ /\ m_{Image}$
$4\ r_g$	Vertical	-0.9	41.10	29.72	0.72
		0.0	40.74	33.17	0.81
		0.9	43.53	36.56	0.84
$8\ r_g$	Vertical	-0.9	51.48	48.13	0.93
		0.0	51.83	47.94	0.92
		0.9	52.02	47.02	0.90
$4\ r_g$	Toroidal	-0.9	43.13	41.97	0.97
		0.0	41.83	43.02	1.03
		0.9	39.28	40.56	1.03
$8\ r_g$	Toroidal	-0.9	48.33	48.47	1.00
		0.0	47.70	48.58	1.02
		0.9	47.07	47.80	1.02

complex or turbulent magnetic field structure appears to be an important contributor to depolarization of the photon ring, the effect is not strongly model-dependent, e.g., the details appear to be less important.

In the case of the hotspot, Table 3 shows that for the spin values and orbital radii considered, we do not find strong depolarization in the photon ring compared to the rest of the image $m_{Ring}/m_{Image} \simeq 0.85$.

4 SUMMARY AND DISCUSSION

We have shown that an optimal subtraction of linear polarized flux images from total intensity images calculated from GRMHD simulations can enhance the photon ring feature when the conditions in the plasma are suitable. The method relies on the fact that both kinds of images are highly correlated, except at the photon ring. The photon ring is preferentially less polarized with respect to the rest of the image.

The latter implies that time variability in the source favours a better extraction of the ring. If the photon ring is the only persistently less polarized image feature, residuals from depolarized pixels in the rest of the image will be suppressed when time-averaging, sharpening the photon ring feature. Given that the black hole mass

sets the length and timescales of the system, compared to Sgr A*, M87* is about a thousand times more massive and a thousand times slower. Time-averaging for Sgr A* could be done within a single day or epoch of observing, while for M87* it would require many observational campaigns spanning months to years.

Extracting the photon ring by subtracting polarized flux requires a prominent photon ring feature in the total intensity image, and fails when regions other than the photon ring are persistently depolarized, e.g., due to self-absorption or Faraday rotation. As a result, the method works best at low to moderate observer inclinations. M87* is known to be viewed at low inclination and viable theoretical models of the EHT image show prominent photon ring features (Gravity Collaboration et al. 2018b, 2020a,c). We present in Fig. 5 the photon extraction technique applied to 230 GHz images of M87*. These snapshots are calculated using the GRMHD simulations described in Section 2. The black hole mass has been scaled to 6×10^9 M$_\odot$ and the total flux at 230 GHz to $0.5 - 1$ Jy. The viewer's inclination is $i = 17°$. It can be seen that the technique works well in these low inclination cases where the photon ring is visible.

Frequency is an important factor as well. At low frequencies where the emission is self-absorbed, and in local thermodynamic equilibrium, the intensity is that of a blackbody. The radiation will tend to be unpolarized not only at the photon ring, but anywhere in the accretion flow where the optical depth is large. In this case, the photon ring will no longer be an outlier and time variability will not improve the residuals image over time since the location of zones with high optical depth will not vary much. Faraday effects will affect the image in a similar manner, becoming stronger with decreasing frequency and introducing depolarization all over the image. Frequencies $\nu \gtrsim 230$ GHz produce even more favourable results. In particular, Fig. 6 shows a sharp ring residual image at 345 GHz for our MAD model.

We have looked into the numerical properties of the photon ring in our GRMHD images. The lower degree of linear polarization with respect to the rest of the image ($\sim 2 - 2.5$ less polarized) is caused by a combination of plasma effects (absorption and Faraday effects), gravitational effects and magnetic field turbulence in the plasma. The method appears to work as well for sample snapshot polarized images (C. J. White, private communication) from Ressler et al. (2020a), where the simulations are initialized from larger scale MHD simulations of accretion onto Sgr A* via magnetized stellar
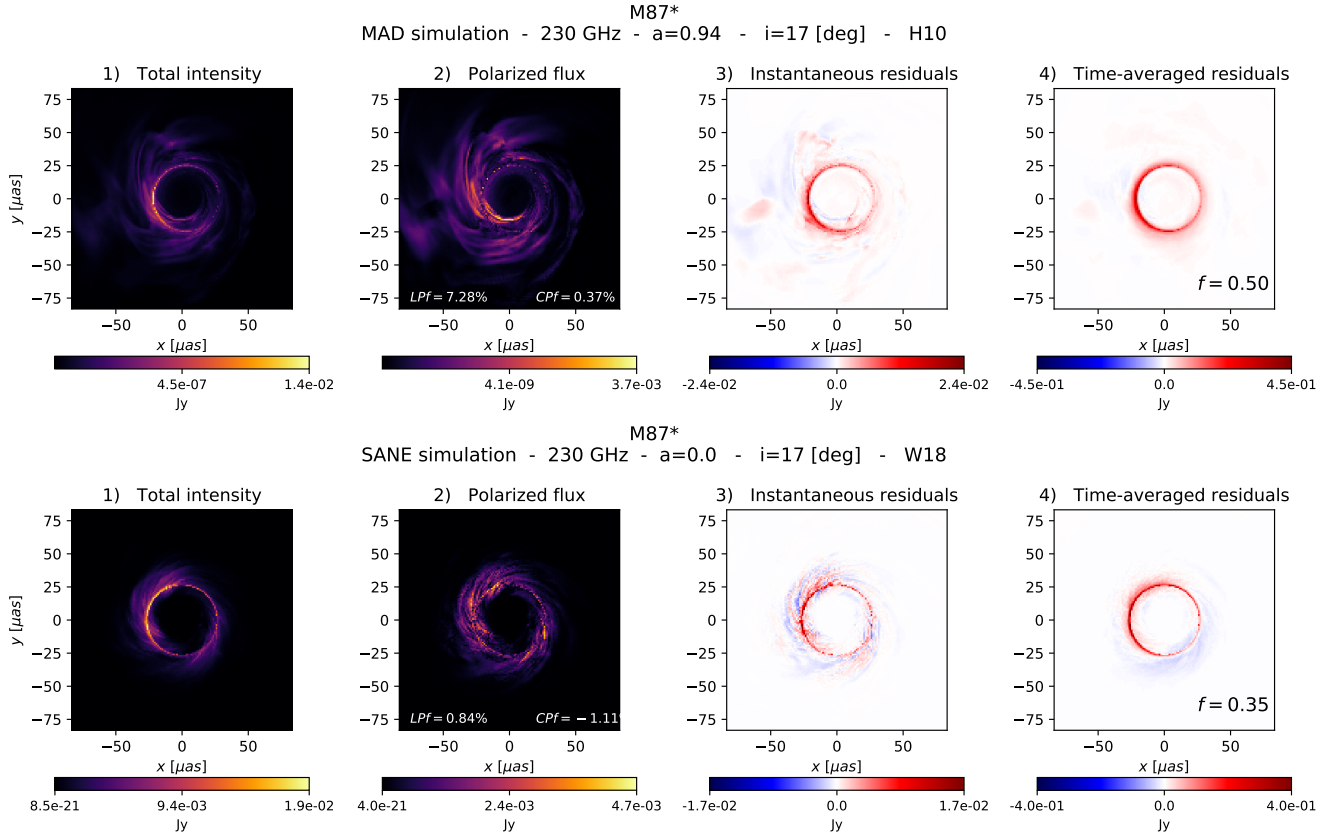
Figure 5. Photon extraction technique applied to 230 GHz images of M87*. The images are calculated from the same GRMHD simulations used for Sgr A*. The black hole mass is scaled to 6×10^9 $M_\odot$ and the total flux to $0.5 - 1$ Jy. The viewer's inclination is $i = 17°$. Total intensity (1), polarized flux (2), instantaneous residuals (3) and time-averaged residuals (4). Top: MAD simulation. Bottom: SANE simulation. In both cases the technique works well for extracting the photon ring.
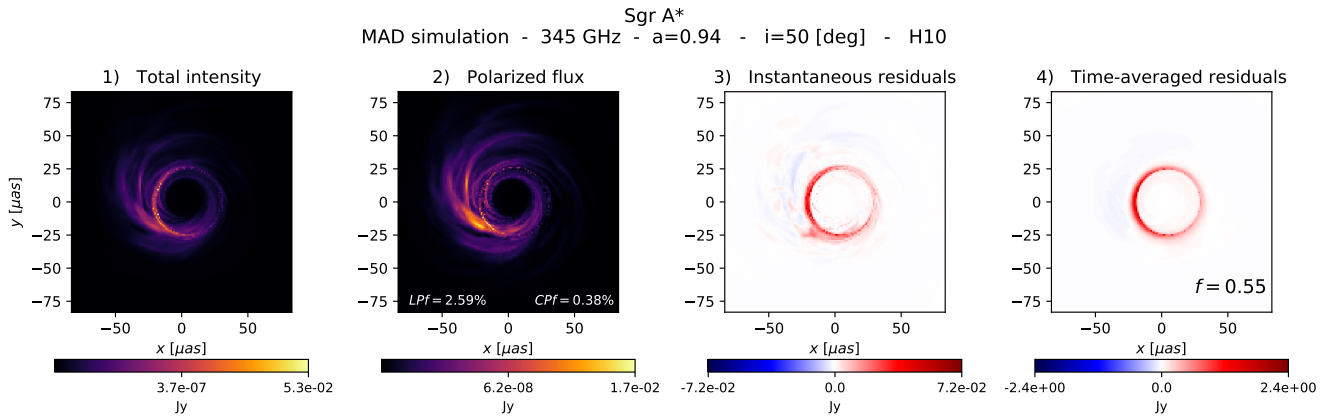
Figure 6. Total intensity (1), polarized flux (2), instantaneous residuals (3) and time-averaged residuals (4) with $f = 0.55$ of images at 345 GHz of the long duration, MAD GRMHD simulation. The net LPf and CPf in the image are indicated in Panel 2. The extraction of the photon ring works better at higher frequency, where other depolarizing effects of self-absorption and Faraday rotation are weaker.

winds. Those simulations show a complex magnetic field structure, where the magneto rotational instabilities are not important at any time (Ressler et al. 2020b). We explore other models in Appendix B and find that the photon ring continues to be less polarized than the rest of the image. An interesting case is shown in Appendix B3, where $m_{\text{Ring}} \lesssim m_{\text{Image}}$, even when all plasma effects are included in the calculations.

the calculations. Understanding when depolarization of the photon ring is seen in GRMHD is an important goal for future work.

We have compared our GRMHD results to those of a semi-analytical hotspot model in idealized magnetic field configurations, different orbital radii and black hole spin. In this case, the results seem consistent with analytic predictions for optically thin emission
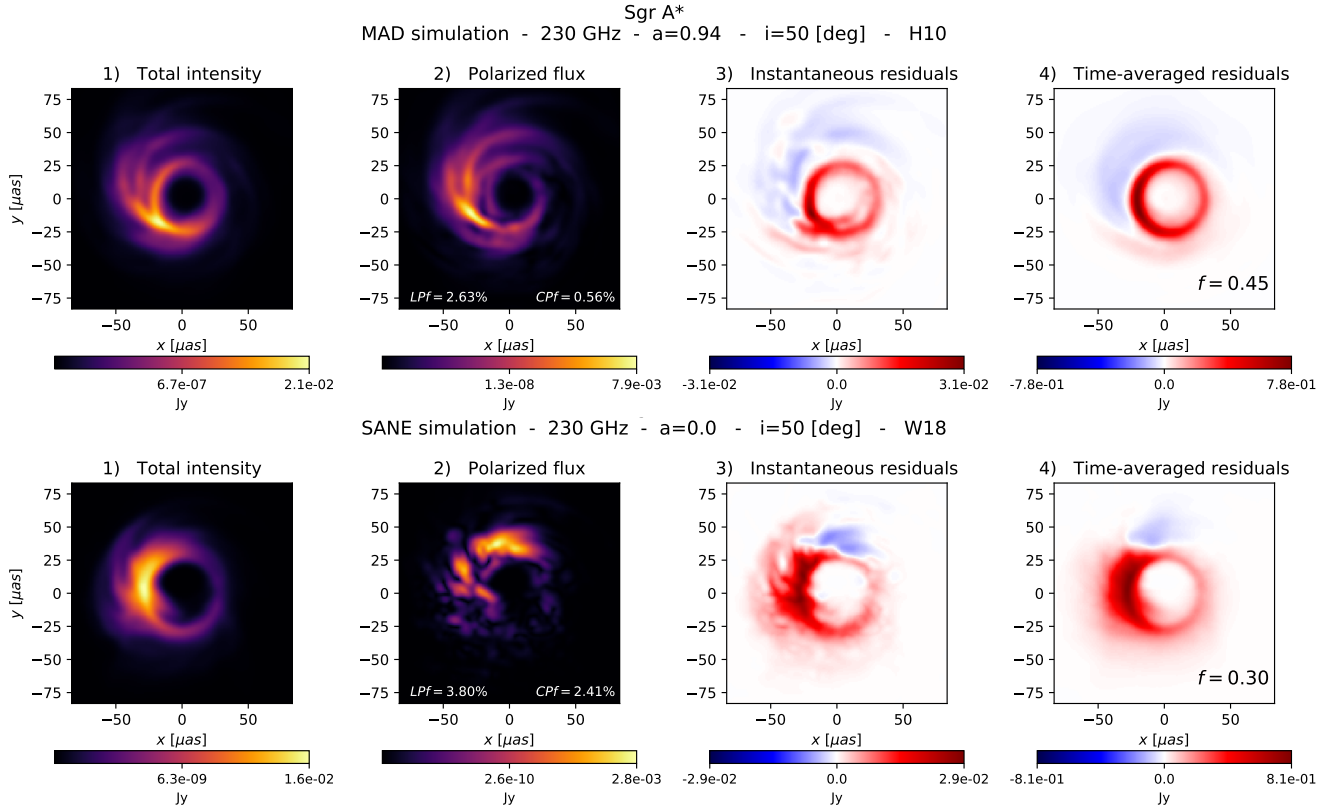
Figure 7. Photon ring extraction technique applied to GRMHD images blurred with a 20μas Gaussian. Top row: MAD simulation. Bottom row: SANE simulation. (1) Total intensity. (2) Polarized flux. (3) Instantaneous residuals. (4) Time-averaged residuals over thirty frames. The technique is still effective for the MAD case. In the SANE case however, the polarized flux image does not show a prominent ring and it is unclear if the ring features in time-averaged residuals are better than the total intensity image.

around black holes (Himwich et al. 2020), where parallel transport is not expected to depolarize emission in the photon ring. Evidently, in addition to plasma effects, both parallel transport and some degree of disorder in the magnetic field configuration are required to cause the depolarization of the photon ring that we find. The results appear insensitive to the model chosen, among the few we have explored.

So far the technique has been presented for the image domain only, using an angular resolution of $\simeq 1\mu$as, far superior to that available with the EHT ($\simeq 10 - 20\mu$as). Given the non-linearity of the polarized flux in terms of the observable Stokes parameters Q and U, an extension to the Fourier domain, where the observables are measured, is non-trivial and is left for future work.

We tried blurring images by convolving the map of each Stokes parameter with a 20μas FWHM Gaussian kernel and then applying the technique. The results are shown in Figure 7. Whereas for the MAD scenario the method still appears to be promising, resulting in a prominent blurred ring, in the SANE case the ring features in the time-averaged residual map do not appear much clearer than in the original total intensity image.

For conditions similar to those found in many viable GRMHD models of Sgr A* and M87*, the relative depolarization of emission from the black hole photon ring may provide a powerful method for extracting it from horizon scale images and movies. The method naturally benefits from the turbulent variability expected from accreting black holes.

DATA AVAILABILITY

The simulated images used here will be shared on reasonable request to the corresponding author.

REFERENCES

Agol E., 2000, ApJ, 538, L121
Aitken D. K., Greaves J., Chrysostomou A., Jenness T., Holland W., Hough J. H., Pierce-Price D., Richer J., 2000, ApJ, 534, L173
Anantua R., Ressler S., Quataert E., 2020, MNRAS,
Bower G. C., Wright M. C. H., Falcke H., Backer D. C., 2003, ApJ, 588, 331
Bower G. C., et al., 2015, ApJ, 802, 69

Bower G. C., Dexter J., Markoff S., Rao R., Plambeck R. L., 2017, ApJ, 843, L31

Bower G. C., et al., 2018, ApJ, 868, 101

Broderick A. E., Loeb A., 2005, MNRAS, 363, 353

Broderick A. E., Loeb A., 2006, MNRAS, 367, 905

Bromley B. C., Melia F., Liu S., 2001, ApJ, 555, L83

Chan C.-K., Psaltis D., Özel F., Narayan R., Sadowski A., 2015, ApJ, 799, 1

Cunningham C. T., Bardeen J. M., 1973, ApJ, 183, 237

De Villiers J.-P., Hawley J. F., Krolik J. H., 2003, ApJ, 599, 1238

Dexter J., 2016, MNRAS, 462, 115

Dexter J., Agol E., 2009, ApJ, 696, 1616

Dexter J., Agol E., Fragile P. C., 2009, ApJ, 703, L142

Dexter J., Kelly B., Bower G. C., Marrone D. P., Stone J., Plambeck R., 2014, MNRAS, 442, 2797

Dexter J., et al., 2020, MNRAS, 494, 4168

Doeleman S. S., et al., 2008, Nature, 455, 78

Doeleman S. S., et al., 2012, Science, 338, 355

Eisenhauer F., et al., 2008, GRAVITY: getting to the event horizon of Sgr A*. p. 70132A, doi:10.1117/12.788407

Event Horizon Telescope Collaboration et al., 2019a, ApJ, 875, L1

Event Horizon Telescope Collaboration et al., 2019b, ApJ, 875, L2

Event Horizon Telescope Collaboration et al., 2019c, ApJ, 875, L3

Event Horizon Telescope Collaboration et al., 2019d, ApJ, 875, L4

Event Horizon Telescope Collaboration et al., 2019e, ApJ, 875, L5

Event Horizon Telescope Collaboration et al., 2019f, ApJ, 875, L6

Falcke H., Melia F., Agol E., 2000, ApJ, 528, L13

Fish V. L., et al., 2011, ApJ, 727, L36

Fishbone L. G., Moncrief V., 1976, ApJ, 207, 962

Gammie C. F., McKinney J. C., Tóth G., 2003, ApJ, 589, 444

Gravity Collaboration et al., 2017, A&A, 602, A94

Gravity Collaboration et al., 2018a, A&A, 615, L15

Gravity Collaboration et al., 2018b, A&A, 618, L10

Gravity Collaboration et al., 2020a, arXiv e-prints, p. arXiv:2002.08374

Gravity Collaboration et al., 2020b, arXiv e-prints, p. arXiv:2004.07187

Gravity Collaboration et al., 2020c, A&A, 643, A56

Himwich E., Johnson M. D., Lupsasca A. r., Strominger A., 2020, arXiv e-prints, p. arXiv:2001.08750

Howes G. G., 2010, MNRAS, 409, L104

Ichimaru S., 1977, in Plasma Physics: Nonlinear Theory and Experiments. pp 262–283

Jiménez-Rosales A., Dexter J., 2018, MNRAS, 478, 1875

Johannsen T., Psaltis D., 2010, ApJ, 718, 446

Johnson M. D., et al., 2015, Science, 350, 1242

Johnson M. D., et al., 2019, arXiv e-prints, p. arXiv:1907.04329

Kuo C. Y., et al., 2014, ApJ, 783, L33

Luminet J. P., 1979, A&A, 75, 228

Marrone D. P., 2006, PhD thesis, Harvard University

Marrone D. P., Moran J. M., Zhao J.-H., Rao R., 2007, ApJ, 654, L57

Mościbrodzka M., Gammie C. F., Dolence J. C., Shiokawa H., Leung P. K., 2009, ApJ, 706, 497

Mościbrodzka M., Dexter J., Davelaar J., Falcke H., 2017, MNRAS, 468, 2214

Narayan R., Yi I., 1994, ApJ, 428, L13

Narayan R., Sadowski A., Penna R. F., Kulkarni A. K., 2012, MNRAS, 426, 3241

Noble S. C., Gammie C. F., McKinney J. C., Del Zanna L., 2006, ApJ, 641, 626

Paumard T., et al., 2008, in Richichi A., Delplancke F., Paresce F., Chelli A., eds, The Power of Optical/IR Interferometry: Recent Scientific Results and 2nd Generation. p. 313, doi:10.1007/978-3-540-74256-2_38

Psaltis D., Özel F., Chan C.-K., Marrone D. P., 2015, ApJ, 814, 115

Quataert E., Gruzinov A., 2000, ApJ, 545, 842

Rees M. J., 1982, in Riegler G. R., Blandford R. D., eds, American Institute of Physics Conference Series Vol. 83, The Galactic Center. pp 166–176, doi:10.1063/1.33482

Ressler S. M., Tchekhovskoy A., Quataert E., Chand ra M., Gammie C. F., 2015, MNRAS, 454, 1848

Ressler S. M., White C. J., Quataert E., Stone J. M., 2020a, arXiv e-prints, p. arXiv:2006.00005

Ressler S. M., Quataert E., Stone J. M., 2020b, MNRAS, 492, 3272

Ricarte A., Dexter J., 2015, MNRAS, 446, 1973

Shiokawa H., 2013, PhD thesis, University of Illinois at Urbana-Champaign

Tchekhovskoy A., 2019, HARMPI: 3D massively parallel general relativictic MHD code (ascl:1912.014)

Tchekhovskoy A., Narayan R., McKinney J. C., 2011, MNRAS, 418, L79

Viergutz S. U., 1993, A&A, 272, 355

Werner G. R., Uzdensky D. A., Begelman M. C., Cerutti B., Nalewajko K., 2018, MNRAS, 473, 4840

Yuan F., Quataert E., Narayan R., 2003, ApJ, 598, 301

APPENDIX A: DEPENDENCE OF RESULTS ON RAY TRACING IMAGE RESOLUTION

We have studied how image resolution affects the results presented in this work. Figure A1 shows distributions of the pixel fractional polarization from one snapshot of the MAD simulation at 230 GHz, at different resolutions. Though there are small differences among the exact values of the net LP, the photon ring pixels show different properties to those of the image pixels, with the photon ring being a factor of $\sim 2 - 2.5$ less polarized. Our results remain qualitatively the same with resolution.

APPENDIX B: PHOTON RING EXTRACTION METHOD IN OTHER MODELS

We apply our extraction method to different models.

B1 Different electron heating

We calculate Sgr A* images at 230 GHz using the same MAD and SANE GRMHD simulations described in Section 2, but consider different electron heating mechanisms: MAD with magnetic reconnection (W18) and SANE with turbulent heating (H10).

Total intensity, polarized flux and residual images are shown in Fig. B1 for both models. In both cases, the photon ring appears as a less polarized feature in the polarized flux images. In the case of the MAD W18 images, the extraction method appears to work well, with a sharp ring feature in the time-averaged residuals. This is not the case for the SANE H10, where it is unclear if photon ring features are sharper than those from total intensity images.

B2 Varying inclinations

We explore different inclinations in Sgr A* images at 230 GHz using our fiducial MAD and SANE GRMHD simulations.

Total intensity, polarized flux and residual images are shown in Figures B2 and B3 for the MAD and SANE models respectively. The photon ring is significantly less polarized. The method works better at lower/moderate inclinations and fails at high inclinations.

B3 MAD with spin a=0.0

We study Sgr A* images calculated from a slightly different GRMHD MAD simulation. Both the images parameters and GRMHD initial conditions remain the same as those described in Section 2 with the only difference that the spin value is $a = 0.0$. Just like in the fiducial MAD simulation, turbulent electron heating (H10) is considered.
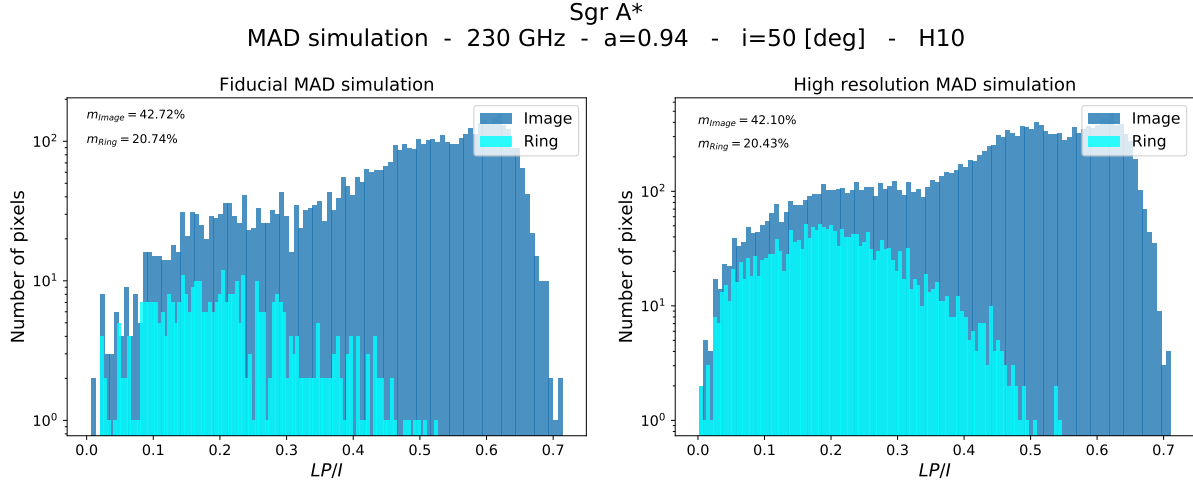
Figure A1. Distribution of LP/I per pixel from one snapshot of the MAD simulation at different resolutions. All plasma effects have been considered in the calculation. Only pixels with a total intensity of at least $10\%\ I_{med}$ are considered, with I_{med} the median of the one hundred brightest pixels. Left: fiducial MAD simulation used in the calculations ($192 \times 192 \times 1600$ pixels, where the latter represents the step size of the geodesic integrator). Right: higher resolution ($384 \times 384 \times 1600$). The net LP of the image and the ring are indicated on each panel. Our results remain qualitatively the same with varying resolution: the photon ring pixels show different properties to the image pixels and are a factor $\sim 2 - 2.5$ less polarized.
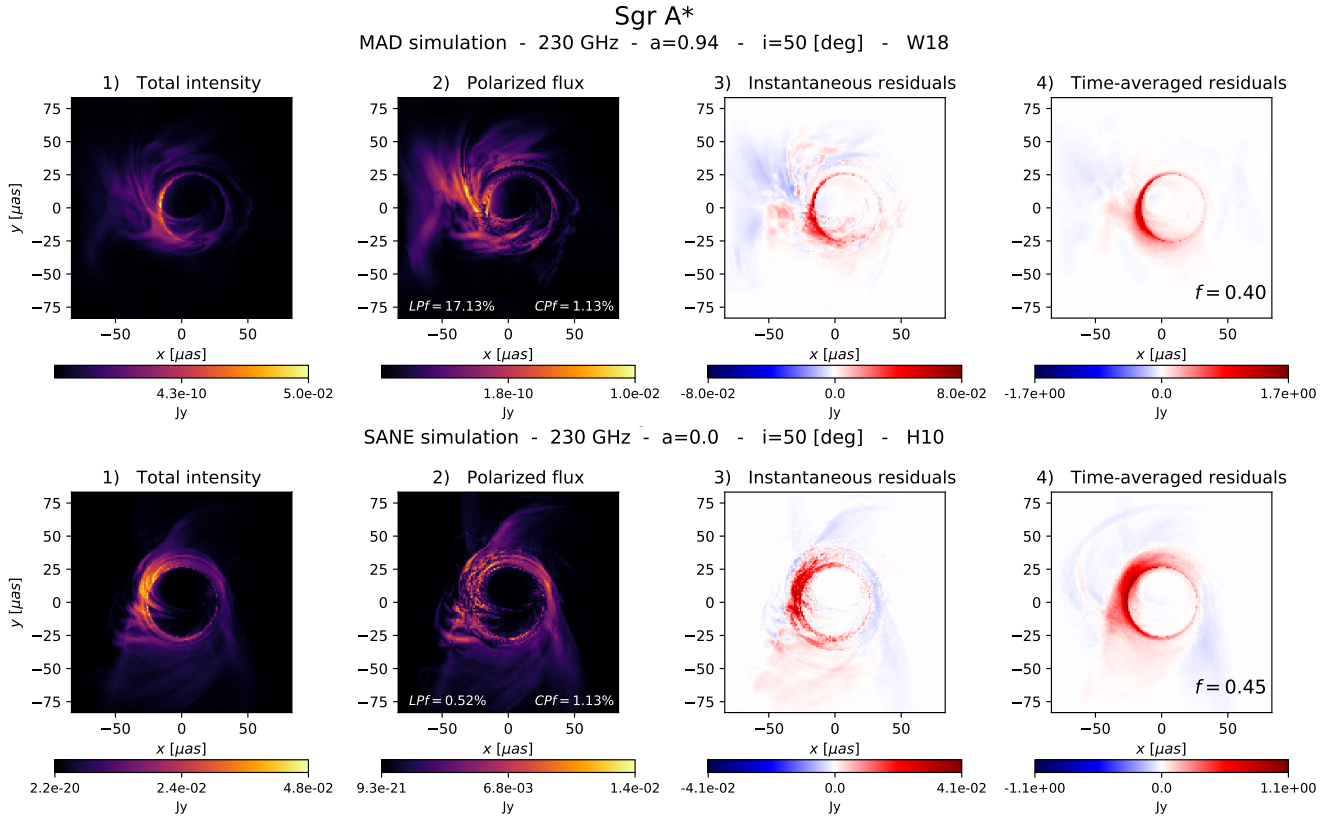

Figure B1. Total intensity, polarized flux and residual images for a Sgr A* model at 230GHz. The images are calculated from a MAD simulation with electron heating from magnetic reconnection (top) and SANE simulation with turbulent heating (bottom). In both cases, the photon ring appears as a less polarized feature in Panel 2. In the case of the MAD W18 images, the extraction method appears to work well, producing a ring with sharper features. This is unclear for the SANE case.
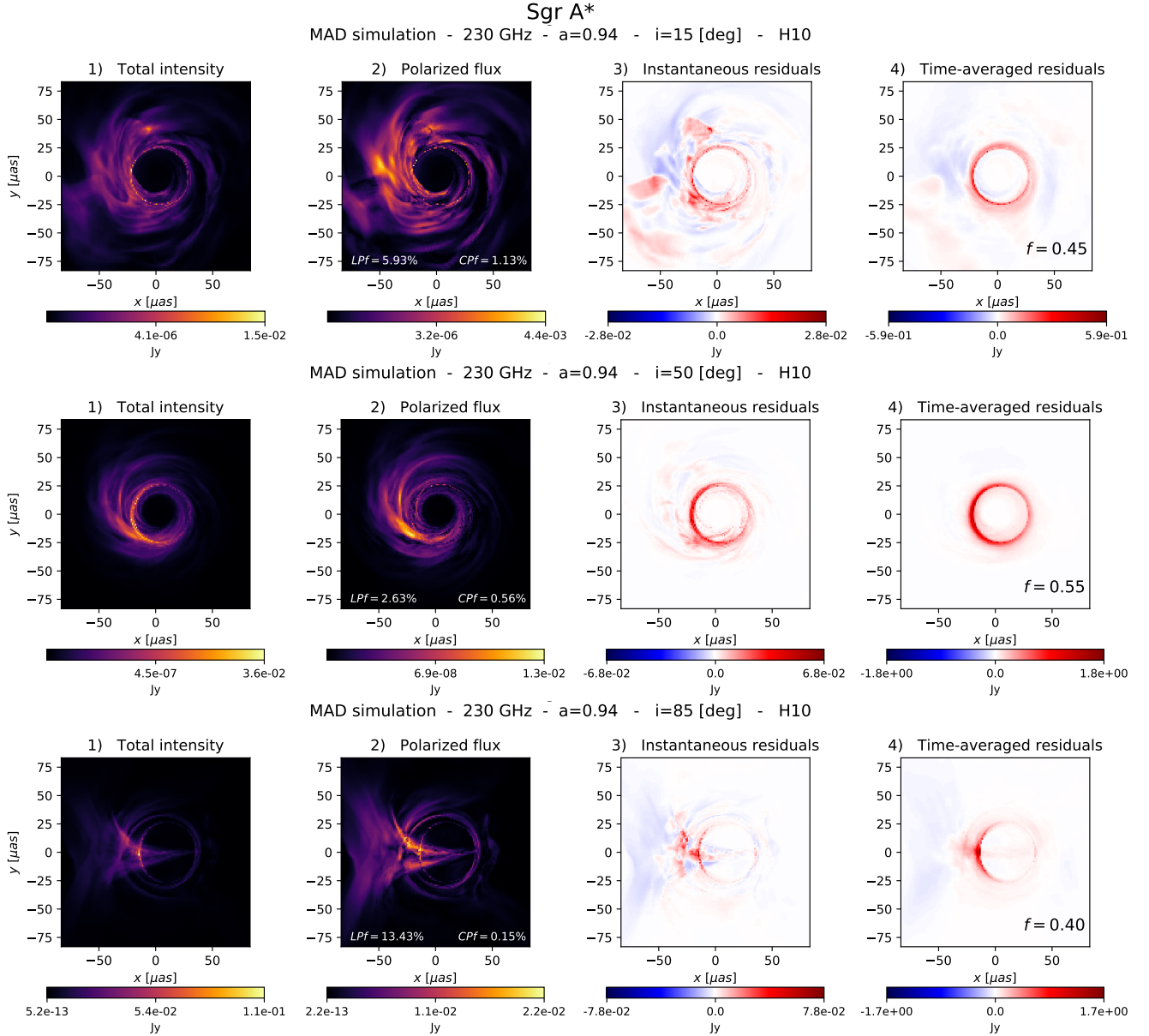
Figure B2. Comparison of Sgr A* images at 230GHz from the fiducial MAD H10 simulation at three different inclinations. Top: $i = 15°$. Middle: $i = 50°$. Bottom: $i = 85°$. The method works better at lower inclinations.

The top panel of Figure B4 presents the photon ring extraction technique applied to these images. In this case it is unclear that the method produces a sharper ring than that obtained directly from total intensity images.

The bottom panel of Figure B4 shows the distribution of the Sgr A* MAD $a = 0.0$ images with all plasma effects included. Both pixel distributions show similar behaviours. Table B1 shows the net LP in the image and ring pixels with a total intensity of at least 10% I_{med}, with I_{med} the median of the one hundred brightest pixels. The photon ring continues to be more depolarized than the rest of the image. However, $m_{\mathrm{Ring}}/m_{\mathrm{Image}} \simeq 0.8 - 0.9$. Plasma effects, particularly absorption, are an important source of depolarization in this case.

This paper has been typeset from a TEX/LATEX file prepared by the author.

Table B1. Net fractional LP (m) for a Sgr A* model using a MAD simulation with spin $a = 0.0$ and turbulent electron heating (H10). The values are calculated from a thirty-frame averaged image including effects of absorption and/or Faraday rotation and conversion at a time.

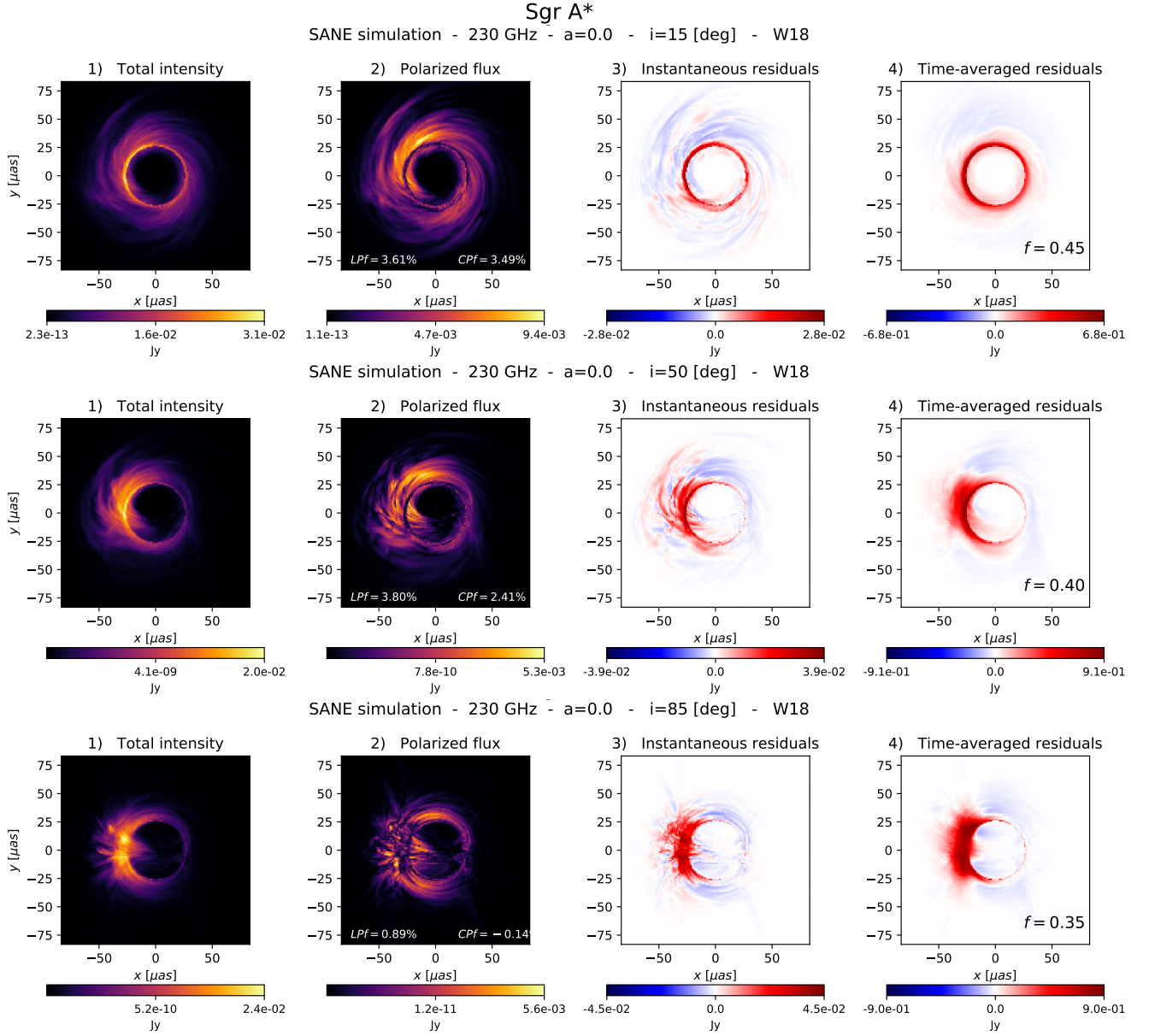|		All effects	No effects	No absorption	No Faraday
MAD	m_{Image} [%]	42.25	48.69	46.50	44.51
a=0.0	m_{Ring} [%]	35.19	44.52	43.56	36.63
	$m_{\mathrm{Ring}} / m_{\mathrm{Image}}$	0.83	0.91	0.94	0.82

Figure B3. Comparison of Sgr A* images at 230GHz from the fiducial SANE W18 simulation at three different inclinations. Top: $i = 15°$. Middle: $i = 50°$. Bottom: $i = 85°$. The method works better at lower inclinations.
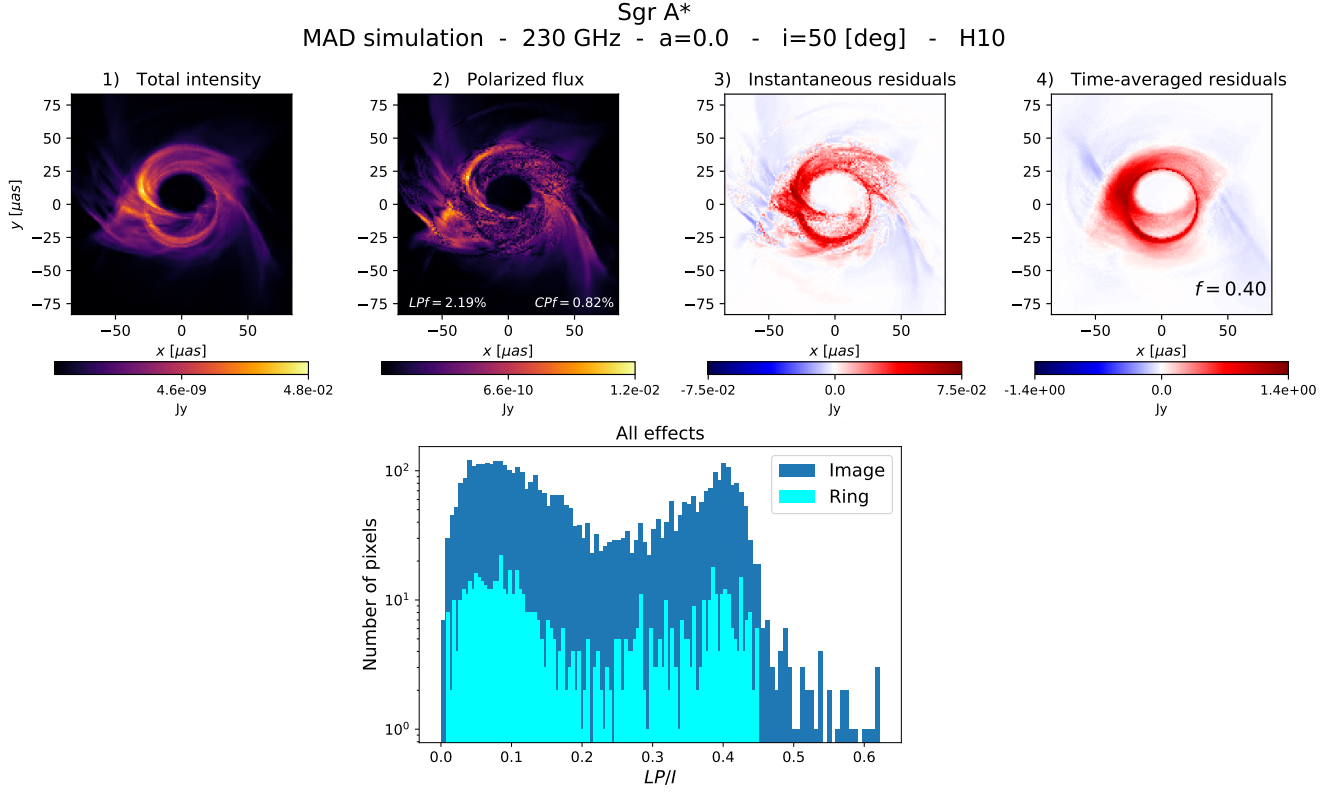
Figure B4. Sgr A* images from a MAD simulation with black hole spin $a = 0.0$. Top: Total intensity, polarized flux, instantaneous residuals and time-averaged residuals. It is unclear that the photon ring is more visible in the time-averaged residual image compared to the total intensity panel. Bottom: distribution of image and ring fractional polarized flux (LP/I) per pixel. Only pixels with a total intensity of at least 10% I_{med} are considered, with I_{med} the median of the one hundred brightest pixels. Image pixels are in dark blue, ring pixels are in cyan. LP/I is calculated from thirty-frame averaged images where all plasma effects are considered.